



## Interaction between swarming active matter and flow: The impact on Lagrangian coherent structures

Xinyu Si  and Lei Fang <sup>\*</sup>*Department of Civil and Environmental Engineering, University of Pittsburgh, Pittsburgh, Pennsylvania 15261, USA*

(Received 8 November 2023; accepted 20 February 2024; published 8 March 2024)

We conducted experiments using a typical centimeter swimmer, *A. salina*, and an electromagnetically driven quasi-two-dimensional flow to study the interaction between active matter and flow. The flow spanned from time-independent cellular flow to weakly time-dependent regimes. We focused on the impact of swarming active matter on hyperbolic Lagrangian coherent structures (LCSs) that mark the most straining regions in the flow. There is one decade of scale separation between active matter agents and the length scale of LCSs. We illustrated that the impact of active matter on LCSs was much more significant compared to localized random noise with similar energy input. In addition, we revealed that the perturbation generated by active matter could couple with the background flow and further deform the LCSs. In addition to the impact on the most straining hyperbolic regions of flow, we also revealed that the rotational elliptical region of the flow was much more susceptible to active matter perturbation in a Lagrangian perspective. We further described how the influence of active matter changed with their number densities and background flow intensities. We revealed that the LCSs could be decently altered even at a small number density of active matter. Through this work, we aim to provide valuable insights and draw attention to the problem regarding the interaction between active matter and external flow structures.

DOI: [10.1103/PhysRevFluids.9.033101](https://doi.org/10.1103/PhysRevFluids.9.033101)

### I. INTRODUCTION

Active matter defines a broad spectrum of subjects that are characterized by the capability of transducing free energy into systematic movements [1]. Under this broad definition, active matter encompasses both living matter and nonliving imitations, ranging from micrometer-scale bacteria to dekameter-scale mammals [2,3]. This comprehensive inclusion of research subjects hence attracted the attention of diverse communities with varying perspectives.

One major perspective focuses on the collective behaviors and self-organization of active matter. It is ubiquitous in natural systems that huge amounts of living matter, such as collections of bacteria and fish schools, exhibit coherent motions and long-range ordering. The analogy between flocking active matter and some condensed matter systems like ferromagnets and liquid crystals [4] has captivated the interest of and spawned extensive investigation within the communities of condensed matter physics and statistical physics. The viewpoint is to regard the collection of active matter as some materials so that the collective behaviors of active matter can be characterized and understood through the adaptation and modification of suitable condensed matter physics theories [5] and hydrodynamics theories [1,6]. Research topics from this perspective are vast and diverse. Some of

---

<sup>\*</sup>lei.fang@pitt.edu

the main research topics include emergent structures, symmetries, phase transitions, and rheological properties [2].

This paper, however, shifts the viewpoint from active matter behaviors to the flow environment they are living in. Active agents consume energy in order to move around and exert mechanical forces on the flow around them [1,2]. Especially for aquatic creatures, the enormous range of body size covered by various aquatic animals and the relatively higher viscosity of liquid than that of air result in the expansive Reynolds numbers for active-matter-induced flow, from Stokes flow to fully developed turbulence [7]. The diverse moving patterns of various species make the classification and characterization of swimmer-generated flows even more challenging and intriguing. There are many investigations conducted just focusing on the locomotion and the detailed description of flows induced by various moving patterns of different species under different regimes of Reynolds numbers [8–12]. Additionally, there are also numerous investigations focused on the impacts of external flow environment on the transport and distribution of swimmers [13–17].

Another considerable portion of investigations focuses on the chaotic flows at very low Reynolds numbers, where inertia effects are negligible [18,19]. These chaotic flows are also known as active turbulence [20]. The constituents of the active matter for active turbulence are mostly microswimmers, such as bacteria [21–23] and tissue cells [24]. The key difference between active turbulence and inertial turbulence is that the active matter is not treated as external forces but rather a component in a continuum description of the flow system. Consequently, the active turbulence is considered as autonomous and self-organized. The investigations of active turbulence are closely related to the research with respect to the collective movements of active matter. Attention is paid to the characterization and classification of the active turbulence under different ordering phases of flocking active matter [20].

The investigation on biologically generated turbulence with higher Reynolds numbers were primarily conducted by the oceanographic community focusing on the mixing effect of aquatic animals. Early stage investigations mainly focused on a bulk estimation of the injected energy by marine animals and hence evaluating their potential on mixing the ocean [7,25,26]. Contrary opinions have been raised [27,28] regarding the mixing effect for low-Reynolds-number swimmers due to their low mixing efficiency. However, mesoscale animals are at least still promising in ocean mixing due to their massive total amounts and the intermediate Reynolds numbers [29]. Additionally, in recent years, it was found that collective motion of centimeter-scale aquatic organisms could form aggregate-scale eddies that could effectively modify the stratification of water columns at much larger length scales [30,31].

Even though much research has been performed on active-matter-induced flow, almost all previous works have considered the active matter as energy sources independently without considering the background flow environment. However, natural water bodies like oceans and lakes are driven by various energy sources and hence the living environment of most aquatic creatures are almost always flowing. The interaction between biologically generated flow and the background flow environment can be a significant factor on influencing the flow environment but has long been overlooked. In our recent research, we performed investigations on the interaction between a biologically generated jet behind a centimeter-scale swimmer and a background shear flow. We found that both the intensity and direction of the biologically generated turbulent energy cascade depended on the geometric configuration between the biologically generated agitation and the background shear. As a result, the background shear could be either intensified or attenuated depending on different tensor geometries [32].

Here, we continue on the investigation about the interaction between active-matter-induced agitations and background flow fields. In this work, we incorporated a typical centimeter-scale swimmer *A. salina*, commonly known as brine shrimp, under swarming movement into an electromagnetically driven quasi-two-dimensional (quasi-2D) cellular flow. By “swarming,” we mean the polarization [33,34] of the group is, on average, zero, and the velocity of the agents are randomly aligned with each other. We focus on the impact of the swarming active matter on Lagrangian coherent structures (LCSs). Different from a Eulerian framework where the properties of flows are defined at points

fixed in space, a Lagrangian framework describes flow properties following the reference frame of individual passive tracers in the flow. We used a Lagrangian framework rather than a Eulerian framework because the Lagrangian framework intrinsically contains information about advection in the flow and hence can provide a better description for the transport and mixing properties of scalars. LCSs characterize the flow in a simpler, lower-order way. They form the skeletons of the flow, where the strongest straining occurs. Hyperbolic LCSs are considered as good detection of transport barriers. Therefore, studying the influence of active matter on LCSs serves as a crucial starting point and provides valuable insights to unravel the complex problem regarding the impact of active matter on the transport and mixing properties of the flow. Direct measurement of the transport and dispersion of scalars in the flow field is beyond the scope of this paper. Further investigations on these aspects will be conducted in follow-up studies.

We start with providing experimental details in Sec. II and Sec. III. Section II describes the experimental methods used to generate and measure the quasi-2D flow as well as the characterization of the generated flow. Section III introduces the animal used in this work called *Artemia salina*. A step by step protocol is provided for the experiments with *A. salina* incorporated. The flows generated by swarming *A. salina* without background flow are characterized in this section. Section IV gives a brief theoretical background review for quasi-2D Navier-Stokes equation and Lagrangian coherent structures. The influence of swarming active matter on LCSs is then presented and discussed in Sec. V, Sec. VI, and Sec. VII. Section V contrasts the active-matter-incorporated flow with the background flow overlaying two different kinds of perturbations: random noise of the same energy input and spatiotemporally correlated perturbations of the same energy input. Through contrasting, we confirm the importance of two different kinds of interactions: one involves the interaction between the flows generated by individual active matter; the other involves the interaction between the active-matter-generated flow and the background flow environment. Section VI probes further onto the question about how the effect of active matter on background flow changes with number density (packing fraction). Section VII, on the other hand, explores how the effect changes with the variation of background flow intensity. Finally, we summarize our findings and draw conclusions in Sec. VIII.

## II. EXPERIMENT: TWO-DIMENSIONAL ELECTROMAGNETICALLY DRIVEN FLOW

The quasi-2D flow as a background for examining the impact of swarming active matter on LCSs was generated by an electromagnetically driven flow system and resolved using a particle tracking velocimetry (PTV) system [35]. The experimental apparatus, particle tracking operations, and some prime characteristics of the flow are introduced successively in this section.

### A. Apparatus

The apparatus for the quasi-2D flow system was composed of a main acrylic body frame, a pair of copper electrodes installed on the opposite sides of the setup, and a piece of tempered glass in the center that separated a thin layer of salt water on top and an array of cylindrical magnets below. A schematic diagram for the setup is shown in Fig. 1. Similar apparatus has been introduced in detail elsewhere [15,36,37]; hence here we only briefly describe the necessary parameters. The dimension of the main body frame and the glass floor in the center were  $96.5 \times 83.8 \text{ cm}^2$  and  $81.3 \times 81.3 \text{ cm}^2$ , respectively. The upper surface of the glass was coated with hydrophobic materials (Rain-X) to reduce friction and the lower surface was covered by light-absorbing blackout film. Beneath the glass, the cylindrical magnet array was organized in checkerboard pattern of alternative polarity with a center-to-center space of  $L_m = 5.1 \text{ cm}$ . Each magnet (neodymium grade N52) had an outer diameter of 1.27 cm and a thickness of 0.64 cm, with the maximum magnetic flux density of 1.5 T at the magnet surface. We loaded a thin layer (6 mm thickness) of 14% by mass NaCl solution on top of the glass. The solution had density  $\rho_f = 1.101 \text{ g/cm}^3$  and viscosity  $\nu = 1.25 \times 10^{-2} \text{ cm}^2/\text{s}$ . By passing a dc current through the conducting solution layer, we were able to drive a quasi-2D flow

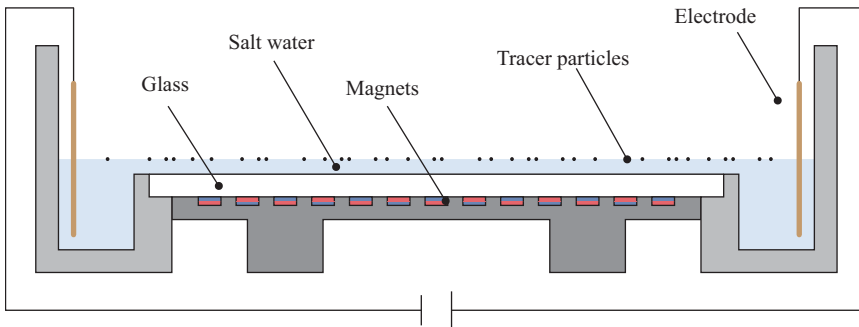


FIG. 1. Schematic diagram of the experimental apparatus.

with the resulting Lorentz body force in horizontal directions and control the flow Reynolds number by adjusting the dc current intensity. It has been shown that, within this electromagnetically driven thin layer system, the flow is nearly 2D when the  $Re$  (essentially the flow velocity) is lower than a critical value [36]. Since the flow velocity in our experiments were lower than the critical value in [36], the 2D condition was well kept throughout our experiments. Note that, under our definition of  $Re$  (see Sec. II C), since the length scale  $L_m$  was arbitrary, the  $Re$  was just a characterization of the flow velocity. In this paper, the  $L_m$  was two times the value used in [36].

### B. Particle tracking and data postprocessing

To track the flow, we seeded the fluid with green fluorescent polyethylene particles (Cospheric) with a density of  $\rho_p$  1.025 g/cm<sup>3</sup> and diameters  $d$  ranging from 106 to 125  $\mu\text{m}$ . We calculate the Stokes number of the tracer particles as

$$St = \frac{1}{18} \frac{\rho_p}{\rho_f} \frac{d^2}{L^2} Re, \quad (1)$$

where  $L$  is the characteristic length scale of the flow field. Taking  $L = L_m$  and the  $Re$  defined in Sec. II C, we can get that the Stokes number of the particles was of order  $10^{-5}$ , which means that the particle could accurately trace the flow [38]. Since the density of the particles was lower than the working fluid, they would float on the gas-liquid interface and show a slow clustering tendency due to surface tension effects, which is known as the ‘‘cheerios effect’’ [39]. To reduce the surface tension, a small amount of surfactant was added to the fluid in order to minimize its impact on the movement of the tracers.

We used a machine vision camera (Basler, acA2040-90  $\mu\text{m}$ ) to image the flow that was illuminated by blue LED lights. A 19.4 cm by 19.4 cm region at the center of the setup was recorded with a resolution of 1600 pixels by 1600 pixels. About 8000 particles could be recorded at a frame rate of 60 frames per second. With this particle density and frame rate, we could obtain a highly spatiotemporally resolved velocity field through a particle tracking velocimetry (PTV) algorithm. For easier use, the measured flow was then interpolated onto regular Eulerian grids using cubic interpolation with a grid size of 15 pixels (1.8 mm), which gave a grid density similar to the original particle density. In 2D, the kinetic energy transfers to larger length scales. In our experiment, the smallest length scale of interest is of similar length as the body length of a single *A. salina*, which is around 1 cm. Using the smallest length scale of interest and the velocity corresponding to the largest  $Re$  in Fig. 2(b), we can get that the time scale of the flow is larger than 1 s. Therefore, the particle density and frame rate is high enough to resolve the flow field of interest.

When the images included both particles and *A. salina*, the pixels corresponding to *A. salina* were premasked before the images were processed by the PTV algorithm. The intensity of these pixels

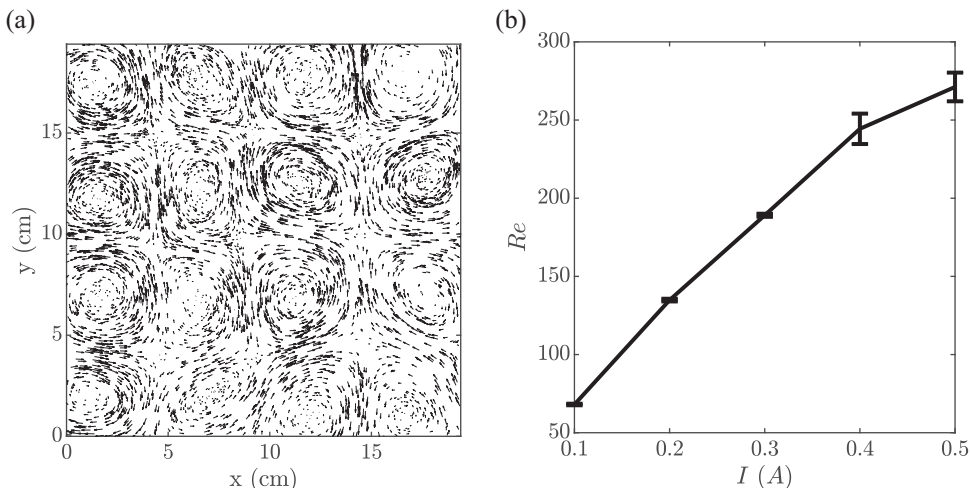


FIG. 2. (a) Snapshot of the measured flow field under 0.3 A dc current. Velocity vectors are downsampled for better visualization. (b) The mean  $Re$  over 5000 frames of the measured flow fields under dc current intensities from 0.1 A to 0.5 A. The error bar represents one standard deviation.

was replaced by the intensity value of the black background so that they would not be detected by the PTV algorithm. Therefore, only the motion of the flow would be tracked.

### C. Flow characterization

In this work, we measured flows under dc current intensities from 0.1 A to 0.5 A with a 0.1 A increment. Under 0.1 A, the flow was a steady laminar cellular flow. As the current intensity increased, the flow gradually became weakly time dependent but was still strongly correlated with the locations of the magnets, where the strongest forcing was located. Figure 2(a) shows a snapshot of the measured flow field under a 0.3 A dc current. It can be noticed that the center-to-center distance between flow cells was the same as  $L_m$ , which was used here as the characteristic length scale of the flow field. The Reynolds number calculated as  $Re = UL_m/\nu$ , where  $U$  is the root-mean-square velocity of the flow field, increased from 68 to 270 with the corresponding dc current intensities [Fig. 2(b)].  $U$  was calculated as  $U = \sqrt{\langle \mathbf{u} \cdot \mathbf{u} \rangle}$ , with the angle bracket  $\langle \cdot \rangle$  representing the ensemble average and  $\mathbf{u}$  representing the full velocity vector.

## III. EXPERIMENT: ACTIVE MATTER

In this work, a typical centimeter-scale animal *Artemia salina*, commonly known as brine shrimp, was used to examine the influence of active matter on LCSs. The typical body length of an adult-sized *A. salina* is about 1 cm [31]. This small animal swims by propelling its pairs of appendages and forms a jet opposite to its swimming direction. Figure 3 shows a snapshot of the flow field around a single *A. salina* swimming in quiescent water. It can be noticed that an *A. salina* can generate flows at length scales much larger than its body length, which creates chances for dynamical interactions with background flow at larger scales. The ensemble average swimming speed of a single *A. salina* was measured to be 0.68 cm/s. The standard deviation of the average swimming speed along individual swimming trajectories was calculated to be 0.41 cm/s. In this section, we will describe in detail the protocol for the experiments with *A. salina* incorporated into the quasi-2D flow. The flows generated by swarming *A. salina* at different packing fractions (PF) are then characterized in Sec. III B.

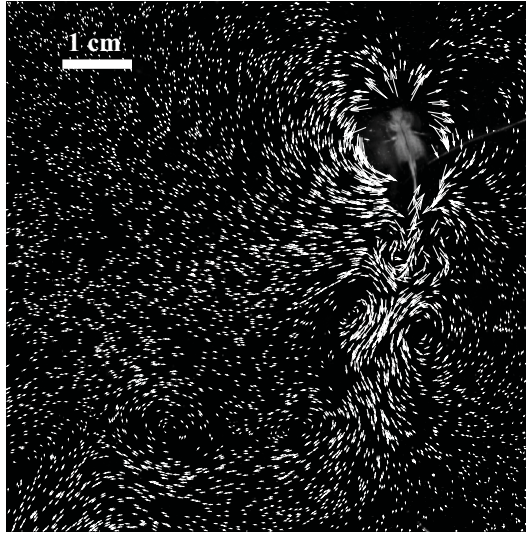


FIG. 3. Image of a single *A. salina* swimming in quiescent water. The vectors mark the flow generated by this *A. salina*. Figure adapted from [32].

#### A. Protocol for experiments with animal

Adult-sized *A. salina* was obtained from the supplier (Northeast Brine Shrimp) and cultured in 3% by mass NaCl solution for at least 24 h before they were introduced to the experiment. Since the culturing fluid was less dense than the working fluid, the *A. salina* would be kept floating on the surface of the working fluid throughout the full experiment period. Sets of experiments with different background flow intensities (dc current intensities) were conducted separately. For each set with the same background flow intensity and different packing fractions of *A. salina*, the series of data were collected following the protocol as below.

- (i) Load the working fluid to the apparatus.
- (ii) Turn on the dc power supply. Adjust the current intensity to the intended magnitude and wait until the flow is fully developed.
- (iii) Record the background flow with constant current intensity for 5000 image frames. [The root-mean-square velocity of the background flow for all sets is shown in Fig. 2(b).]
- (iv) Turn off the dc power supply. Record the decaying flow with enough time length. This is used to calculate the bottom friction coefficient  $\alpha$  [40] (see Sec. IV A).
- (v) Introduce a suitable amount of *A. salina* to the working fluid and wait until the animals spread out and reach a statistically stationary state. Record the flow with the introduced *A. salina* with no background flow for 5000 image frames.
- (vi) Turn on the dc power supply. Adjust the current intensity to the intended magnitude and wait until the flow is fully developed. Record the flow with the introduced *A. salina* and background flow for 5000 image frames.
- (vii) Turn off the dc power supply and let the flow decay.
- (viii) Repeat steps (v) to (vii) by gradually introducing more *A. salina* to the working fluid until a desired high density of *A. salina* is reached.

#### B. Swarming-*A. salina*-induced flow characterization

Since the light environment for the experiment was uniformly deployed, the *A. salina* had no directional bias and showed a swarming movement pattern. As is shown in Fig. 4(a), the  $u$  component and  $v$  component of the flow field show exactly the same distribution for all selected



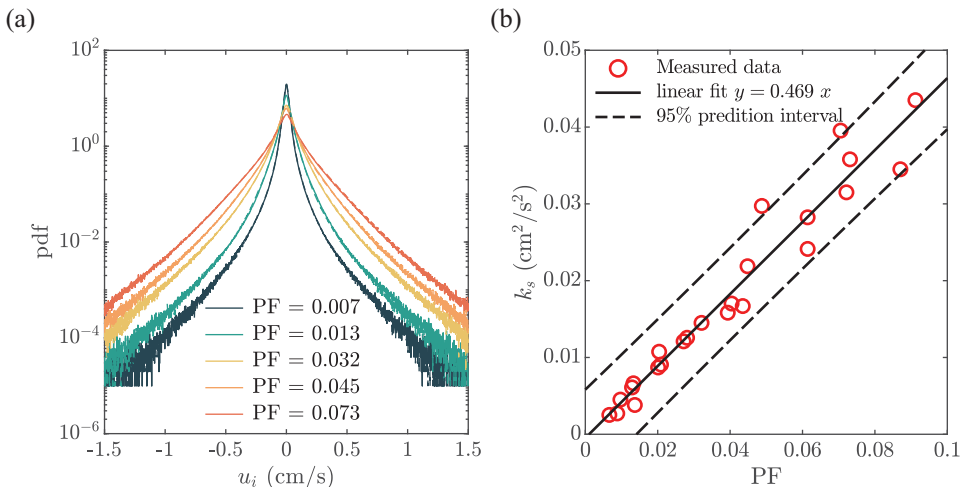


FIG. 4. (a) Velocity component magnitude distribution for the flow field with different selected packing fractions (PF) of *A. salina* and no background flow. The  $u$  components are plotted in solid lines and the  $v$  components are plotted in dashed lines. However, since the two lines are highly overlapped, the dashed line becomes less discernible. This means that both components with the same PF show the same distribution, which implies that the movements of *A. salina* have no directional bias. (b) Turbulent kinetic energy  $k_s$  of flow generated by swarming *A. salina* at different PF. Red circles represent measured data for all sets. The solid line shows the least squares regression of the data and the dashed line gives the 95% prediction interval (two standard deviations).

packing fractions, where  $u$  and  $v$  are velocity components of two perpendicular axes of the 2D flow field. The flow field induced by swarming *A. salina* was strongly non-Gaussian with a heavy long tail, indicating the occurrence of remarkable rare events. We also examined how the turbulent kinetic energy of the flow would increase with the packing fraction (PF) of *A. salina*. Here, in two dimensions, PF is defined as the ratio of the area occupied by *A. salina* to the total area of the image domain. Therefore, PF serves as a direct measure of the number density of *A. salina* in the flow field. In Fig. 4(b), we show the data measured in step (v) of Sec. III A for all sets of experiments [since step (v) was conducted without dc current, the experimental condition could be considered as the same for all sets of experiments at this step] together with the list squares regression. We found that the swarming-*A. salina*-induced turbulent kinetic energy  $k_s = \frac{1}{2}(\mathbf{u}' \cdot \mathbf{u}')$  increased linearly with the packing fraction of *A. salina*, where the  $\mathbf{u}'$  is the fluctuation velocity and here, due to the swarming movement,  $\mathbf{u}'$  equals the full velocity  $\mathbf{u}$ . This indicates that the flow kinetic energy induced by individual *A. salina* can be linearly added together to approximate the total kinetic energy yielded by swarming groups. Consequently, the turbulent kinetic energy at any packing fraction of *A. salina* between 0 and 0.1 can be estimated by interpolation.

#### IV. THEORETICAL BACKGROUND

##### A. Two-dimensional Navier-Stokes equation

The equation of motion for incompressible flow in two dimensions is [41]

$$\partial_t \mathbf{u} + \mathbf{u} \cdot \nabla \mathbf{u} = \nabla p / \rho + \nu \Delta \mathbf{u} + \mathbf{f} + \alpha \mathbf{u}, \quad (2)$$

where  $\mathbf{u}$  is the velocity,  $p$  is the pressure, and  $\mathbf{f}$  is an external force term that drives the flow. Specifically,  $\alpha$  is the coefficient corresponding to linear damping. Since, in 2D flow, kinetic energy cascades toward larger scales rather than small scales [42], the linear damping term dominates the energy dissipation process in 2D, as opposed to the viscous dissipation term in three dimensions

(3D). In our experiment, the linear damping mainly results from the bottom friction. Without external forces and only focusing on the kinetic energy contained in the flow system under linear damping, we get  $\partial_t \mathbf{u} = \alpha \mathbf{u}$  and we will, therefore, expect an exponential decay of the kinetic energy. The linear damping coefficient  $\alpha$  can then be estimated by measuring a decaying flow [40]. In this work,  $\alpha$  values were measured at the start of each set of experiments [see Sec. III A, step (iv)]. The mean value of  $\alpha$  was measured to be  $-0.074 \text{ s}^{-1}$ , with one standard deviation at  $0.009 \text{ s}^{-1}$ .

### B. Lagrangian coherent structures and finite-time Lyapunov exponent

Flows show coherence ubiquitously. The coherent structures—macroscopic regions in the flow that show distinguishable spatial and temporal correlations—are hence significant in characterizing complex flows in a simpler lower-order way. Compared to Eulerian coherent structures, such as vortices, detecting coherent structures in a Lagrangian way, that is, following the paths of tracers in the flow, inherently shows many advantages because it accounts for the effects of advection. Lagrangian coherent structures (LCSs), as described by [43], are regions in the flow that mark the most repelling, attracting, and shearing material surfaces. Since the LCSs detect the most straining regions in the flow, they are considered as effective representations of transport barriers in the flow that is crucial for transportation and mixing processes. In 2D, due to the inverse energy cascade, the LCSs are more robust than in 3D, which makes the 2D flow a good test system for investigating LCSs dynamics.

One of the most commonly used methods for detecting LCSs is the finite-time Lyapunov exponent (FTLE). In two dimensions, we calculate FTLE following the method in [43]. The flow gradient  $\nabla F_{t_0}^t(\mathbf{x}_0)$  is first calculated using a finite-difference approximation as

$$\nabla F_{t_0}^t(\mathbf{x}_0) \approx \begin{pmatrix} \frac{x(t;t_0, \mathbf{x}_0 + \delta_1) - x(t;t_0, \mathbf{x}_0 - \delta_1)}{2|\delta_1|} & \frac{x(t;t_0, \mathbf{x}_0 + \delta_2) - x(t;t_0, \mathbf{x}_0 - \delta_2)}{2|\delta_2|} \\ \frac{y(t;t_0, \mathbf{x}_0 + \delta_1) - y(t;t_0, \mathbf{x}_0 - \delta_1)}{2|\delta_1|} & \frac{y(t;t_0, \mathbf{x}_0 + \delta_2) - y(t;t_0, \mathbf{x}_0 - \delta_2)}{2|\delta_2|} \end{pmatrix}, \quad (3)$$

where  $F_{t_0}^t(\mathbf{x}_0) = \mathbf{x}(t; t_0, \mathbf{x}_0)$  is the flow map that depicts the transport of a fluid element from an initial position  $\mathbf{x}_0$  at time  $t_0$  to the position  $\mathbf{x}$  at time  $t$ . The  $\delta_1$  and  $\delta_2$  are two vectors pointing in horizontal ( $x$ ) and vertical ( $y$ ) directions, respectively, that represent small perturbations. The right Cauchy-Green strain tensor

$$C(\mathbf{x}_0) = [\nabla F_{t_0}^t(\mathbf{x}_0)]^T \nabla F_{t_0}^t(\mathbf{x}_0) \quad (4)$$

depicts how an initially small perturbation at  $\mathbf{x}_0$  evolves with time. The eigenvalues  $\lambda_i(\mathbf{x}_0)$  and eigenvectors  $\xi_i(\mathbf{x}_0)$  of this symmetric and positive definite tensor satisfy

$$C\xi_i = \lambda_i \xi_i, \quad i = 1, 2, \quad 0 < \lambda_1 < 1 < \lambda_2, \quad \xi_1 \perp \xi_2. \quad (5)$$

The FTLE is then calculated as

$$\text{FTLE}(\mathbf{x}_0) = \frac{1}{t - t_0} \ln \sqrt{\lambda_2(\mathbf{x}_0)}. \quad (6)$$

Repelling FTLE ( $\text{FTLE}^+$ ) is calculated by integrating in forward time ( $t_0 < t$ ). The regions with local maximum values usually occur along ridges and the ridges are interpreted as effective detection of repelling LCSs. Attracting FTLE ( $\text{FTLE}^-$ ), on the other hand, is calculated by integrating in backward time ( $t_0 > t$ ). Since  $\text{FTLE}^-$  is negative, regions with local minimum values then form ridges that are the locations of attracting LCSs [14]. By integration, we mean the calculation of the Lagrangian trajectories of the tracers from their initial locations  $\mathbf{x}_0(t_0; t_0, \mathbf{x}_0)$  to the final locations  $\mathbf{x}(t; t_0, \mathbf{x}_0)$ , requiring the integration of local flow velocity as  $\mathbf{x} = \mathbf{x}_0 + \int_{t_0}^t \mathbf{u}(\tau, \mathbf{x}) d\tau$ . We conducted the integration using a second order Runge–Kutta scheme implemented in Matlab.

In this work, we took the magnitude of both  $\delta_1$  and  $\delta_2$  to be 15 pixels (1.8 mm). The flow was integrated by two eddy turnover time ( $L_m/U$ ) for each set of experiments. Figure 5(a) shows a



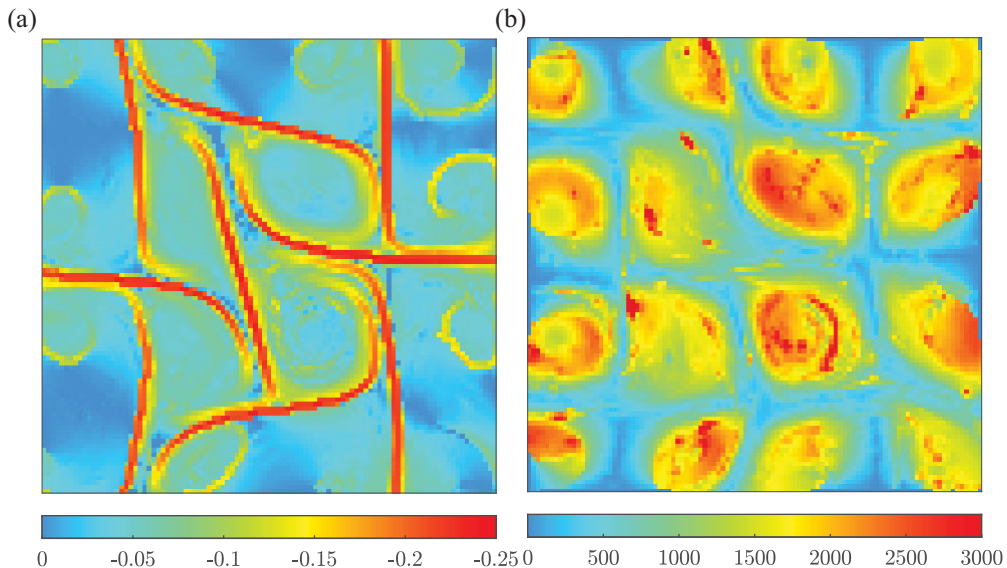


FIG. 5. (a) Snapshot of one frame of attracting FTLE calculated with the flow under 0.3 A dc current. The flow was integrated by two eddy turnover time. The unit of the FTLE is  $s^{-1}$ . (b) Snapshot of the LAVD for the same flow field in (a) at the same moment. The flow was integrated by one eddy turnover time. LAVD is dimensionless.

snapshot of attracting FTLE (FTLE<sup>-</sup>) for the flow under 0.3 A dc current intensity. The FTLE<sup>-</sup> ridges mark the most straining hyperbolic regions that separate the elliptical islands.

Additionally, Ref. [44] also introduced Lagrangian-averaged vorticity deviation (LAVD) to detect rotationally coherent vortices. In 2D, the LAVD is calculated as

$$\text{LAVD}_{t_0}^t(\mathbf{x}_0) = \int_{t_0}^t |\omega(\mathbf{x}(s; \mathbf{x}_0), s) - \bar{\omega}(s)| ds, \quad (7)$$

where  $\omega$  is the vorticity and  $\bar{\omega}$  is the instantaneous spatial mean of  $\omega$ . Figure 5(b) displays a snapshot of the LAVD field for the same flow field in Fig. 5(a) at the same moment. The flow was integrated by one eddy turnover time. By examining the FTLE field and LAVD field of a flow, we can characterize the straining hyperbolic regions and the rotating elliptical regions and explore how these regions change with additional external forces.

## V. IMPACT OF ACTIVE MATTER ON LAGRANGIAN COHERENT STRUCTURES—DESCRIBE BY CONTRASTING

The incorporation of active matter into an existing flow field introduces extra energy and new boundary conditions, as well as new time and length scales. The profound complexity of the system makes a clear understanding of the full dynamical process extremely challenging. Therefore, in this section, we choose to first describe the influence of active matter on LCSs by contrasting it with the influence of two other kinds of perturbations: overlaid random noise of the same kinetic energy and overlaid spatiotemporally correlated perturbations of the same kinetic energy. The hope is that, by contrasting with the influence of other kinds of perturbations, we can gain insights into the impact of active matter on LCSs. While it is challenging to fully comprehend what the influence “is,” we can at least acquire some knowledge about what it “is not.” In this and the next section, we focus on the set of data measured with  $I = 0.3$  A. Specifically, from now on, we call the flow that actually embedded the active matter “active-matter-incorporated flow” contrasting to the cases where the

flow's Eulerian velocity fields were overlaid with perturbation velocity fields. In addition, the LCSs in our flow had a length scale of roughly 10 cm and the *A. salina* had a length scale of 1 cm.

A good starting point is to compare the impacts generated by perturbations from *A. salina* with those from local random noise. One of the most significant differences between these two conditions is that the perturbations from *A. salina* have spatiotemporal correlations. As is mentioned in Sec. III, the perturbation generated by a single *A. salina* is in the form of a jet opposite to its swimming direction. The jets generated by swimming *A. salina* interact with each other and also interact with the background flow. These interaction processes persist in time and could form large scale flow structures, introducing extra time and length scales. Local random noise, on the other hand, does not have any spatial or temporal correlations. By comparing these two conditions, we can reveal the importance of the new time and length scales introduced by active matter. The local random noise was generated with random directions and constant magnitude. In Fig. 4(b), we characterized the linear relationship between the packing fraction of *A. salina* and the turbulence kinetic energy  $k_s$  generated by *A. salina*. Therefore, the magnitude of the random noise corresponding to a certain packing fraction could be acquired through the list squares regression line in Fig. 4(b). Next, we overlaid the generated random noise to the measured background flow field [the background flow field was measured in step (iii) of Sec. III A]. We then integrated the resulting flow field to obtain the FTLE<sup>-</sup> fields. Figures 6(d)–6(f) show the snapshots of FTLE<sup>-</sup> fields at the same moment with increasing packing fractions at 0.02, 0.04, and 0.08. The corresponding  $k_s$  normalized by the mean flow energy  $\bar{E} = \frac{1}{2}\langle \mathbf{u} \rangle \cdot \langle \mathbf{u} \rangle$  for the background flow field were 0.086, 0.18, and 0.36, respectively. The increase in perturbation intensity created a diffusionlike effect that made the FTLE<sup>-</sup> ridges slightly smear out. However, the essential structure of the LCSs was not affected at all. On the opposite, incorporating *A. salina* into the flow yielded remarkably contrasting results. Figures 6(a)–6(c) show the snapshots of FTLE<sup>-</sup> fields with measured packing fractions of *A. salina* at 0.014, 0.029, and 0.074. The ratio of the turbulence kinetic energy  $k_s$  to the mean flow energy  $\bar{E}$  were 0.076, 0.15, and 0.39, respectively. With the increase of number density of *A. salina*, the LCSs were significantly distorted. The FTLE<sup>-</sup> ridges exhibited a more intricate and twisting configuration. The large LCS structures also diverged intensively from the original cellular form. From this contrast, it shows clearly that the perturbations induced by active matter are completely different from local random noise of similar energy. With the same intensity of  $k_s$ , active matter yielded a much more dramatic influence on twisting and deforming the LCSs than local random noise. The spatial and temporal correlation involved in the active-matter-induced perturbation played a significant role in altering the LCSs of the flow. As is shown in Fig. 3, a single *A. salina* can generate flow structures larger than its own body length. The integral length of the flow field generated by swarming *A. salina* in quiescent water was calculated to be 0.9 cm, which is significantly larger than the correlation length of local random noise.

The comparison with local random noise demonstrates the important role played by the spatiotemporal correlations in the perturbations created by active matter. This spatiotemporal correlation results from the interactions between large scale flow structures. However, considering the condition where the movements of active matter are incorporated into the background flow, the interaction not only occurs among active-matter-induced flows, but also occurs between the active-matter-induced flows and the background flow field. Through the next contrast between the active-matter-incorporated flow and the background flow directly overlaying the active-matter-induced flow in quiescent water, we will show that the interaction between the active-matter-induced flow and the background flow is also a non-negligible factor on shifting and twisting LCSs.

We used the flow fields measured at step (v) in Sec. III A and directly overlaid them onto the background flow field measured at step (iii). The overlaid flow field included the information from both the background flow and the swarming-active-matter-induced flow. Actually, at the same packing fraction, the turbulence kinetic energy was similar no matter whether the active matter was overlaid or incorporated [Fig. 7(a)]. The subtle difference here is that the overlaid case does not have “real” dynamics about the interaction between active-matter-induced flows and the background

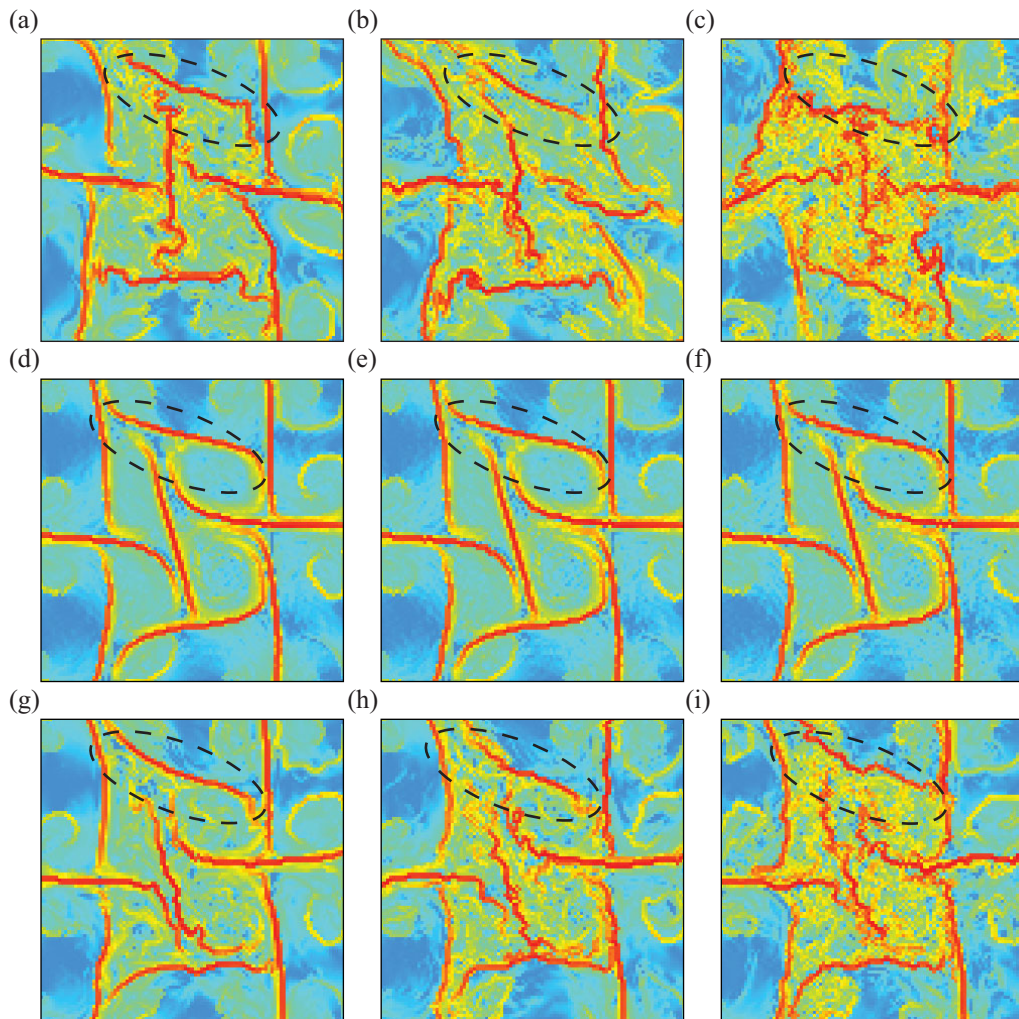


FIG. 6. Panels (a)–(c) give snapshots of  $\text{FTLE}^-$  fields with *A. salina* incorporated into the background flow. The packing fractions of *A. salina* are (a) 0.014, (b) 0.029, and (c) 0.074. The corresponding  $k_s/\bar{E}$  are 0.076, 0.15, and 0.39, respectively. Panels (d)–(f) give snapshots of  $\text{FTLE}^-$  fields with local random noise overlaid to the background flow. The packing fractions selected for obtaining  $k_s$  are (d) 0.02, (e) 0.04, and (f) 0.08. The corresponding  $k_s/\bar{E}$  are 0.086, 0.18, and 0.36, respectively. The relationship between packing fraction and  $k_s$  is determined by Fig. 4(b). Panels (g)–(i) give snapshots of  $\text{FTLE}^-$  fields with *A. salina* generated flow in quiescent water overlaid to the background flow. The packing fractions of *A. salina* are (g) 0.013, (h) 0.032, and (i) 0.073. The corresponding  $k_s/\bar{E}$  are 0.063, 0.14, and 0.36, respectively. By saying “overlaid,” we mean the random noise in (d)–(f) and the *A. salina* generated flow in quiescent water in (g)–(i) were first numerically added to the measured background flow field before determining the  $\text{FTLE}^-$  fields. The incorporation cases yield stronger shifting and twisting effects on LCSs. The reader can use the  $\text{FTLE}^-$  ridges in the circled region to compare the differences. The color bar range is the same as Fig. 5(a).

flow. Considering the dynamics in a spectral view may make the difference between these two cases clearer. The background flow had an energy injection length scale  $L_m$  and the kinetic energy shall be mainly stored in large scale eddies having length scales greater than  $L_m$  because the quasi-2D flow system had a net inverse energy flux. The flow induced by *A. salina*, however, had a much smaller

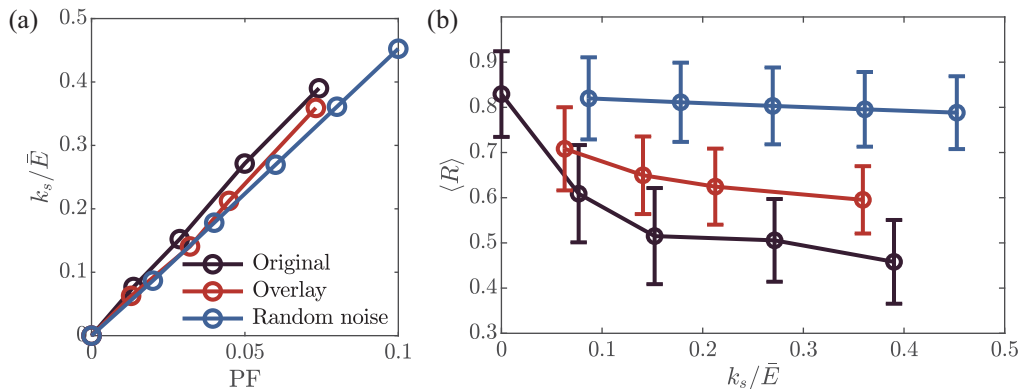


FIG. 7. (a) Ratio of the swarming-active-matter-induced turbulent kinetic energy  $k_s$  to the mean kinetic energy of the background flow  $\bar{E}$  at different packing fractions (PF) for the original active-matter-incorporated flow (black line), the background flow overlaying the active-matter-induced flow in quiescent water (red color), and the background flow overlaying local random noise. (b) The mean correlation coefficient  $\langle R \rangle$  of FTLE<sup>-</sup> fields at different kinetic energy ratio  $k_s/\bar{E}$ . The mean is calculated for all possible pairs of FTLE<sup>-</sup> fields within all one eddy turnover time (7.5 s) windows. The FTLE<sup>-</sup> fields have 100 frames in total with 0.5 s time interval. The error bar shows one standard deviation. Different colors represent the same condition as (a).

energy injection length scale than the background flow. Therefore, the flow measured for swarming *A. salina* in quiescent water shall have main dynamics at smaller length scales. The overlaying of these two flow fields included the dynamics for both flow fields but was lacking the dynamics induced by the direct interaction between active-matter-induced flows and the background flow. Through this contrast, we intend to isolate the dynamics that occurred at the length scales between the energy injection length scale of the background flow and the energy injection length scales of the swarming-active-matter-induced flow. The dynamics that occurred at these length scales were attributed to the interaction between the flow induced by the swarming active matter and the background flow field.

Figures 6(g)–6(i) show the snapshots of FTLE<sup>-</sup> fields at the same moment with measured packing fractions of *A. salina* at 0.013, 0.032, and 0.073. The corresponding  $k_s/\bar{E}$  ratios were 0.063, 0.14, and 0.36, respectively. It can be noticed by comparing the two overlaying cases that overlaying the swarming-active-matter-induced flow created a much more remarkable effect on deforming the LCSs than overlaying local random noise, which again confirms the importance of the spatiotemporal correlation involved in the swarming-active-matter-induced flow. But comparing the second overlaying case, the active-matter-incorporated flow cases [Figs. 6(a)–6(c)] have more shifted and twisted LCSs. To further quantify the degree of deformation on LCSs, for each case, we calculated the FTLE<sup>-</sup> fields every 30 frames (0.5 s) for 3000 frames (50 s) of data and then quantified the mean correlation coefficient  $\langle R \rangle$  for all possible pairs of FTLE<sup>-</sup> fields within one-eddy-turnover-time windows in the same group of data. For example, the correlation coefficient  $R_{A,B}$  between FTLE<sup>-</sup> field *A* and FTLE<sup>-</sup> field *B* was calculated as

$$R_{A,B} = \frac{\text{cov}(A, B)}{\sigma_A \sigma_B}, \quad (8)$$

where  $\text{cov}(A, B)$  is the covariance of *A* and *B* and  $\sigma_A$  and  $\sigma_B$  are the standard deviation of *A* and *B*.  $\langle R \rangle$  was calculated as the mean of all calculated  $R_{A,B}$  values in the same group of data. The parameter  $\langle R \rangle$  quantifies the degree of deformation on LCSs as time progresses. Since the background flow was weakly time dependent, when the time interval between frame *A* and frame *B* was large, the correlation became weak for all groups. Therefore, we let the time interval between *A* and *B* not be larger than one eddy turnover time. As is shown in Fig. 7(b), incorporating swarming *A. salina*



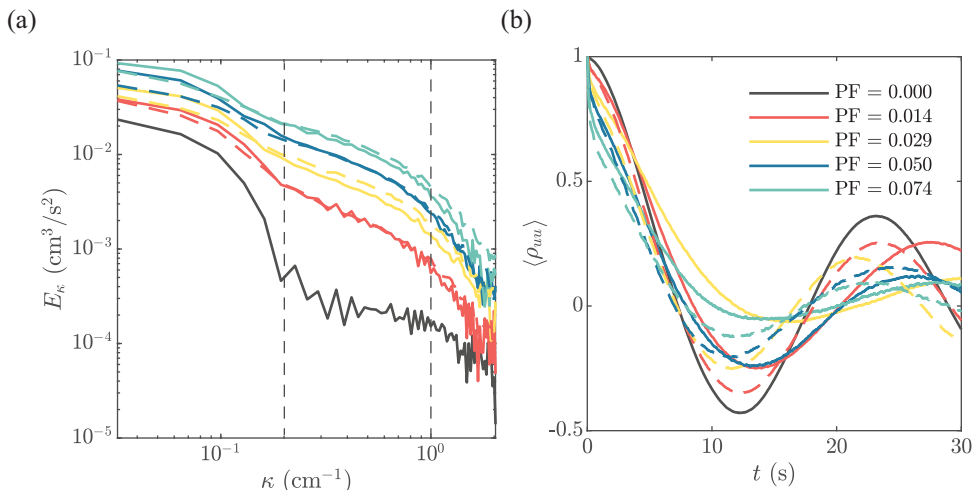


FIG. 8. (a) Turbulence kinetic energy spectrum for the *A. salina*-incorporated flow (solid line) and the background flow overlaying the swarming-*A. salina*-induced flow in quiescent water (dashed line). The packing fraction for each case is the same as (b). The left vertical dash line marks the energy injection length scale of the quasi-2D flow system  $L_m$ . The right vertical dash line marks the length scale of a single *A. salina*. (b) Lagrangian velocity correlation for the *A. salina*-incorporated flow (solid line) and the overlaying flow (dashed line).

yielded the strongest deformation. The local random noise, however, created a minor influence on LCSs with the increase of turbulence kinetic energy.

Figure 7(b) reveals the importance of two different dynamical interactions. The first interaction involves the interaction between the flows induced by individual active matter. The second interaction involves the interaction between the swarming-active-matter-induced flow and the background flow field. Both interactions play a non-negligible role in influencing the formation of LCSs. To further illustrate the second kind of interaction, we performed spectral analysis and Lagrangian statistics for both the active-matter-incorporated flow and the background flow overlaying swarming-*A. salina*-induced flow. As was discussed above, pure swarming-active-matter-induced flow in quiescent water exhibited a smaller characteristic length scale than the background flow. The interaction between these two flows, however, could yield flow structures on scales larger than the pure swarming flow. From Fig. 7(a), we see the turbulence kinetic energy  $k_s$  was the same for both cases. This indicates different spectral distributions of  $k_s$  for these two cases. The active-matter-incorporated flow should have a higher portion of  $k_s$  stored at larger scales than the overlaid case. This inference was confirmed by Fig. 8(a). The case that incorporated *A. salina* did exhibit higher spectral energy than the overlaid case at lower wave numbers  $\kappa$  and lower spectral energy than the overlaid case at higher wave numbers. This difference was not salient, though, because of the limited amount of energy introduced by the active matter. However, the redistribution of energy is consistently observed in all packing fractions. The small amount of energy redistribution notwithstanding, it is surprising that such a subtle difference in power spectrum could result in such pronounced differences in LCSs structures [Fig. 7(b)].

Figure 8(b) essentially reveals the same physics as Fig. 8(a). In this figure, we show the mean Lagrangian velocity correlation  $\langle \rho_{uu} \rangle$  of the velocity component  $u$ . For each tracer starting from the initial location  $\mathbf{x}_0(t_0; t_0, \mathbf{x}_0)$  and following a Lagrangian trajectory as  $\mathbf{x}(t; t_0, \mathbf{x}_0)$ ,  $\rho_{uu}$  was calculated as [45]

$$\rho_{uu}(t) = u(\mathbf{x}(t; t_0, \mathbf{x}_0))u(\mathbf{x}(t_0; t_0, \mathbf{x}_0)). \quad (9)$$

Compared with the overlaid case,  $\langle \rho_{uu} \rangle$  decreased slower in the active-matter-incorporated flow at the initial stage but displayed a weaker periodicity over longer distances. The  $\langle \rho_{uu} \rangle$  decreased slower at the initial stage means the tracers had a longer “memory,” which indicates the stronger correlation at larger length scales, which results from the interaction between the active-matter-induced flow and the background flow. On the other hand, the weaker periodicity over long distances indicates a more intensive deformation and distortion on the LCSs. Due to the coupling between the active-matter-induced flow and the background flow, more fluid particles were dispersed in long-range transport and diverged from the periodic movements in the vortices, which indicated a stronger mixing.

## VI. IMPACT OF ACTIVE MATTER ON LAGRANGIAN COHERENT STRUCTURES—EFFECT OF DIFFERENT PACKING FRACTIONS

In the previous section, we contrasted the *A. salina*-incorporated flow with the background flow overlaying both random noise and swarming-*A. salina*-induced flow field in quiescent water. Through contrast, we revealed the importance of two kinds of interactions in the active-matter-incorporated flow, which resulted in a stronger deformation effect on LCSs than the other two overlaying cases. In this section, we probe deeper into the active-matter-incorporated flow and examine how the effect of active matter on background flow changes with their packing fractions.

The background cellular flow can be categorized into two different regions: the hyperbolic regions and the elliptical regions. The hyperbolic regions exhibit the strongest stretching and compressing, which consequently have the strongest mixing [46]. These regions can be identified by hyperbolic LCSs. The elliptical regions, on the other hand, are dominated by rotational movement. If we use the  $\text{FTLE}^-$  field to identify these two regions, the  $\text{FTLE}^-$  ridges with the lowest values should mark the hyperbolic LCSs. The elliptical regions, due to their rotational movement, should have higher  $\text{FTLE}^-$  values. Note that  $\text{FTLE}^-$  values are negative. Thus lower values mean stronger straining.

To examine the impact of swarming *A. salina* on the flow, we calculated the probability density function (PDF) of the  $\text{FTLE}^-$  fields at different packing fractions of *A. salina*. As is shown in Fig. 9(d), for the background flow (black line) without *A. salina*, there are two distinct peaks. The higher peak with larger  $\text{FTLE}^-$  values represents the elliptical regions that occupy most of the regions in the flow. The lower peak, characterized by smaller  $\text{FTLE}^-$  values, represents the hyperbolic regions. As the packing fraction of *A. salina* increases, the peak corresponding to the elliptical regions drops substantially and spreads out simultaneously. The  $\text{FTLE}^-$  value corresponding to the hyperbolic regions also moves to a lower value but in a much weaker extent than the elliptical region. This change indicates that, from a Lagrangian perspective, the elliptical regions were substantially disturbed by the movement of *A. salina*, even at a very small packing fraction. To further confirm the change in the elliptical region, we calculated the LAVD field for the *A. salina*-incorporated flow. Figures 9(a)–9(c) show the snapshots of the LAVD fields for the same flow field in Figs. 6(a)–6(c) at the same moment. It can be noticed that the elliptical islands marked by higher LAVD values were broken at even low packing fractions of *A. salina*. Note that here the strong disturbance in the elliptical islands is in a Lagrangian perspective. From an Eulerian perspective, the structure of the periodic cells is still mostly intact. This also shows the advantages of using a Lagrangian framework in this work rather than a Eulerian framework. The peak corresponding to the hyperbolic regions, on the other hand, does not exhibit a change as strong as the elliptic regions. It shifts slightly toward a higher  $\text{FTLE}^-$  value and has small changes in peak value. This does not mean, however, the hyperbolic regions were not affected by the movement of *A. salina*. Even though the hyperbolic regions were not broken as strongly as the elliptic regions (in a Lagrangian perspective), they were deformed and twisted by the *A. salina*-induced fluctuations, as was demonstrated by  $\text{FTLE}^-$  ridges in Figs. 6(a)–6(c), indicating a stronger mixing.

Therefore, a relatively more comprehensive picture of how swarming active matter affects the flow field with the increase of packing fraction can be depicted as follows: under low packing



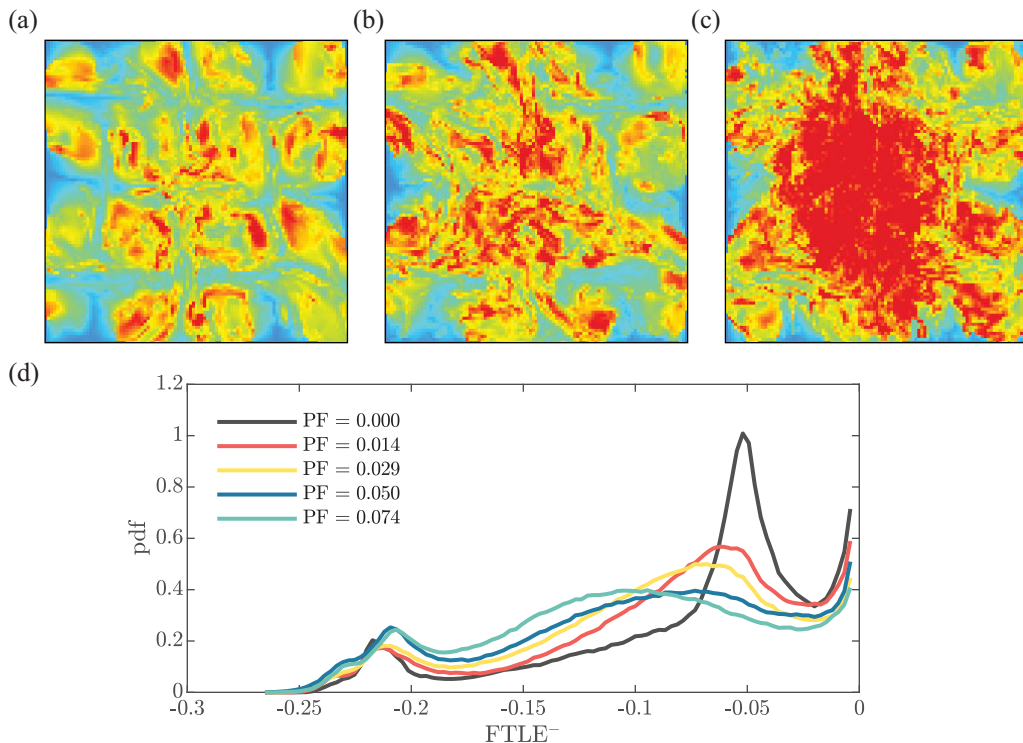


FIG. 9. Panels (a)–(c) give a snapshot of the LAVD field for the same flow as Figs. 6(a)–6(c) at the same moment. The flow was integrated by 7.5 s, which was one eddy turnover time. The color bar range is the same as Fig. 5(b). Panel (d) gives the pdf of  $\text{FTLE}^-$  values for *A. salina*-incorporated flow with different packing fractions (PF).

fractions, the rotational elliptic regions are first disturbed; regions within each elliptical island acquire a more intensive mixing effect. The hyperbolic regions are not significantly affected under low packing fractions of active matter and hence still work as transport barriers between elliptical islands. As the packing fraction of active matter increases, the elliptical regions are totally broken in a Lagrangian perspective. Fluid is intensively mixed up in elliptical regions. The hyperbolic regions are shifted and twisted due to the increasing fluctuation introduced and gradually become less efficient in working as transport barriers, which indicates stronger mixing.

## VII. VARIATION OF BACKGROUND FLOW INTENSITY—THE IMPACT OF $k_s/\bar{E}$

The preceding two sections illustrated how the active matter and their interactions with background flows played a significant role in impacting the deformation of LCSs and how the effect varied with the change of their packing fractions. The analysis in these sections was based on the data measured under  $I = 0.3$  A. Under this background flow intensity, the maximum ratio between the turbulent kinetic energy induced by active matter  $k_s$  and the mean kinetic energy of the background flow  $\bar{E}$  was approximately 0.4. In this section, we continue the investigation by comparing the data measured under varied dc current intensities. The hope is to push the condition to a lower  $k_s/\bar{E}$  ratio and identify active-matter-dominated and flow-dominated regimes based on  $k_s/\bar{E}$ .

We followed the method used in Sec. V and calculated  $\langle R \rangle$  of  $\text{FTLE}^-$  fields within one-eddy-turnover-time windows as the measure of LCSs deformation. The results are presented in Figs. 10(a) and 10(b). Figure 10(a) shows directly all experimentally measured data points. These data points

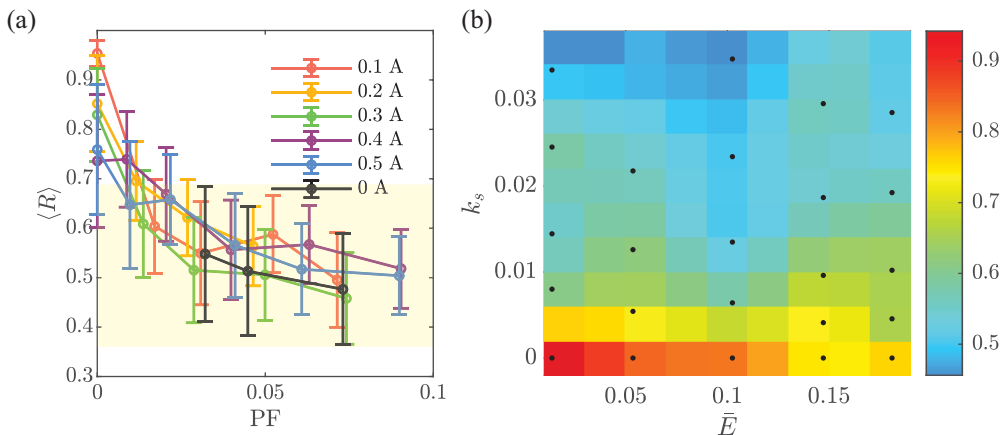


FIG. 10. (a) Mean correlation coefficient  $\langle R \rangle$  of FTLE<sup>-</sup> fields under different background flow intensities. The legend shows the dc current intensities that drove the flows. The error bar represents one standard deviation. The shaded area marks the range of  $\langle R \rangle$  covered by pure active matter cases in quiescent water. Panel (b) gives the 2D map of  $\langle R \rangle$  interpolated from the data in (a). The black points mark the measured data. The  $k_s$  values were obtained through the least squares regression line in Fig. 4(b).

were interpolated onto a 2D map with  $k_s$  and  $\bar{E}$  being two axes in Fig. 10(b). We recall that  $k_s$  and PF have a linear relationship for  $\text{PF} < 0.1$ . The  $k_s$  values in Fig. 10(b) were obtained through the least squares regression line in Fig. 4(b).

There are two factors that can impact the  $\langle R \rangle$ . The first is the impact of active matter. As we observe in Figs. 10(a) and 10(b),  $\langle R \rangle$  decreases as the packing fraction increases at all current intensities. Second, the flow becomes more and more time dependent as the current increases. Even with no active matter (zero packing fraction),  $\langle R \rangle$  has a decreasing trend as dc current intensity increases.

The cases with  $\text{PF} \approx 0.02$  ( $k_s \approx 0.01$ ) are the smallest PF cases that we have besides the pure flow case ( $\text{PF} = 0$ ). In these cases, we see a noticeable drop in  $\langle R \rangle$  and we already observe a decent amount of twisting in the LCSs (see Fig. 6). The minimum ratio of the measured  $k_s/\bar{E}$  under this PF is around 5% with 0.5 A dc current intensity and, as indicated by the notable drop in  $\langle R \rangle$ , we have already approached a visible change in LCSs. This result suggests that, to reach the flow-dominated regime, the flow must contain very weak active matter, where the  $k_s/\bar{E}$  ratio should be much smaller than 5%.

To explore the active-matter-dominated regime, we calculated the  $\langle R \rangle$  for cases when the active matter was in quiescent fluid, where active matter dominated by definition. We did not consider the cases where the PFs were too small because the flow fields in those cases had a large portion of negligible velocity magnitudes that will contaminate the following calculation of the FTLE field. We observe that, in all measured cases, as PF increases,  $\langle R \rangle$  approaches the value for the cases of pure active matter [the shaded area in Fig. 10(a)]. The smallest ratio of  $k_s/\bar{E}$  in the shaded area is around 10%. That is the case with the 0.5 A current ( $\bar{E} \approx 0.2$ ) and packing fraction of around 0.04 ( $k_s \approx 0.02$ ). Unobservantly, one may assume flow transition to the active-matter-dominated regime as  $k_s/\bar{E}$  grows above 10%. However, this conclusion may be flawed because the time dependence of the flow can also contribute to the lower  $\langle R \rangle$ . We can imagine increasing the dc current to an extremely high value, in which case we can confidently say the external flow dominates the process. But the  $\langle R \rangle$  value will also drop simultaneously. When we examine the change of  $\langle R \rangle$  as a function of PF, we will see that, at  $\text{PF} = 0$ ,  $\langle R \rangle$  is already low and close to the shaded area. We cannot conclude that the flow is active-matter dominated in this case. To eliminate the time dependency, we now focus on 0.2 A cases where the cellular structure strictly holds. (We did not use 0.1 A cases because

the smallest measured packing fraction had already entered the active-matter-dominated regime and we could not determine the threshold for the active-matter-dominated regime.) We observe that the smallest  $k_s/\bar{E}$  ratio for  $\langle R \rangle$  to enter the shaded area is around 25%.

Because of the flow's time dependence as we increase the driving force, a clear separation between the flow-dominant regime and active-matter-dominant regime under very intensive and even turbulent background flow cannot be resolved in this work and is pending further exploration. Nevertheless, we can make two conclusions. First, the incorporation of active matter, even at a very low  $k_s/\bar{E}$  (as low as 5% in our experiments), can yield a sharp drop of  $\langle R \rangle$  and the flow leaves the flow-dominated regime. Therefore, it would be expected that the flow-dominated regime exists when  $k_s/\bar{E} \ll 5\%$ . Second, we reveal that the flow is active matter dominated when  $\langle R \rangle \geq 25\%$ , as  $\langle R \rangle$ , in this case, is indistinguishable from the  $\langle R \rangle$  of the pure active matter case.

### VIII. SUMMARY AND CONCLUSIONS

We conducted experiments to study the interaction between swarming active matter and an external background flow field. In this work, we focused on the impact of swarming active matter on LCSs. *A. salina*, a kind of centimeter-scale swimmer, was used as the proxy of active matter and we introduced it into an electromagnetically driven quasi-2D cellular flow with LCSs length scale of around 10 cm. Both the number density of active matter and the dc current intensity were varied so that a broad range of  $k_s/\bar{E}$  ratio was covered, where  $k_s$  is the active-matter-induced turbulent kinetic energy and  $\bar{E}$  is the mean kinetic energy of the background flow.

We illustrated the significance of two different kinds of interaction in impacting the deformation of LCSs by comparing the active-matter-incorporated flow with the background flow overlaying two different kinds of fluctuations. The first interaction involves the interaction between the flow produced by the agitations of individual active matter. The second interaction involves the interaction between the active-matter-induced flow and the background flow field. Both interaction processes play non-negligible roles in shifting and twisting the LCSs.

We further investigated the impact of active matter under different packing fractions. We found that, in a Lagrangian perspective, the elliptical regions in the flow were first disturbed and gradually broken even at a small active matter packing fraction. The hyperbolic regions that worked as transport barriers of the flow were more robust and would not be totally broken by the agitations of active matter. However, this did not mean that hyperbolic regions were not affected. They exhibited strong deformation, characterized by strong shifting in positions and twisting in structures, as the packing fraction of active matter increased. This, by definition, indicated a facilitated mixing effect.

Finally, we explored the effect of active matter on LCSs with varied background flow intensities. We found that the active matter could yield deformation of LCSs even at very low  $k_s/\bar{E}$  ratios (5%). The flow-dominated regime exists when  $k_s/\bar{E} \ll 5\%$ . In addition, we reveal that active matter starts to dominate when  $k_s/\bar{E} \geq 25\%$ . Our result suggests the possibility of breaking transport barriers and facilitating mixing through active matter in natural and industrial flows, such as forbidden zones in the coastal area [47]. This paper reported the kinematics due to incorporating active matter in a background. The detailed dynamics of how an individual swimmer interacts with background flow is also reported in a current paper [32].

Even though the dynamics of active matter have been extensively investigated from various perspectives, their interaction with an existing background flow field has long been overlooked. We hope that this work could provide insights into this problem and draw attention to the interaction between active matter and external flow structures.

Direct measurements of the mixing properties of the flow were not conducted in this work. Despite a strong indication in the facilitated mixing by the strong deformation of LCSs, it is still necessary to perform corresponding statistics to build the connection between the degree of deformation of LCSs and the intensity of mixing.

We also note that the swimming behavior of the active matter may possibly be affected in some way by the imposed flow due to reasons such as rheotaxis. Previous numerical studies have shown

that LCSs' impact on swimmers is small if the swimming speed is larger than the background flow [14]. For this reason, the rheotaxis is not examined in this work, but it expects further exploration and might need to be taken into consideration in future investigations. Furthermore, as the background flow intensity increases, the existence of transport barriers will surely affect the movement of active matter [14,15]. In this regime where the impact of active matter on transport barriers will circle back to the transport of active matter itself, the spatial distribution of active matter, coupled with the alteration of the external flow environment, is also an interesting two-way coupling question that deserves to be explored.

#### ACKNOWLEDGMENT

This work was supported by the U.S. National Science Foundation under Grant No. CMMI-2143807.

- 
- [1] S. Ramaswamy, The mechanics and statistics of active matter, *Annu. Rev. Condens. Matter Phys.* **1**, 323 (2010).
  - [2] M. C. Marchetti, J.-F. Joanny, S. Ramaswamy, T. B. Liverpool, J. Prost, M. Rao, and R. A. Simha, Hydrodynamics of soft active matter, *Rev. Mod. Phys.* **85**, 1143 (2013).
  - [3] M. Brambilla, E. Ferrante, M. Birattari, and M. Dorigo, Swarm robotics: a review from the swarm engineering perspective, *Swarm Intell.* **7**, 1 (2013).
  - [4] J. Toner, Y. Tu, and S. Ramaswamy, Hydrodynamics and phases of flocks, *Ann. Phys. (NY)* **318**, 170 (2005).
  - [5] K. van der Vaart, M. Sinhuber, A. M. Reynolds, and N. T. Ouellette, Mechanical spectroscopy of insect swarms, *Sci. Adv.* **5**, eaaw9305 (2019).
  - [6] N. Bain and D. Bartolo, Dynamic response and hydrodynamics of polarized crowds, *Science* **363**, 46 (2019).
  - [7] M. E. Huntley and M. Zhou, Influence of animals on turbulence in the sea, *Mar. Ecol. Prog. Ser.* **273**, 65 (2004).
  - [8] E. Lauga, Bacterial hydrodynamics, *Annu. Rev. Fluid Mech.* **48**, 105 (2016).
  - [9] J. S. Guasto, R. Rusconi, and R. Stocker, Fluid mechanics of planktonic microorganisms, *Annu. Rev. Fluid Mech.* **44**, 373 (2012).
  - [10] G. V. Lauder and P. G. Madsen, Fish locomotion: kinematics and hydrodynamics of flexible foil-like fins, *Exp. Fluids* **43**, 641 (2007).
  - [11] J. Sznitman, X. Shen, R. Sznitman, and P. E. Arratia, Propulsive force measurements and flow behavior of undulatory swimmers at low reynolds number, *Phys. Fluids* **22**, 121901 (2010).
  - [12] X. N. Shen and P. E. Arratia, Undulatory swimming in viscoelastic fluids, *Phys. Rev. Lett.* **106**, 208101 (2011).
  - [13] S. A. Berman, J. Buggeln, D. A. Brantley, K. A. Mitchell, and T. H. Solomon, Transport barriers to self-propelled particles in fluid flows, *Phys. Rev. Fluids* **6**, L012501 (2021).
  - [14] X. Si and L. Fang, Preferential alignment and heterogeneous distribution of active non-spherical swimmers near lagrangian coherent structures, *Phys. Fluids* **33**, 073303 (2021).
  - [15] X. Si and L. Fang, Preferential transport of swimmers in heterogeneous two-dimensional turbulent flow, *Phys. Rev. Fluids* **7**, 094501 (2022).
  - [16] B. Qin and P. E. Arratia, Confinement, chaotic transport, and trapping of active swimmers in time-periodic flows, *Sci. Adv.* **8**, eadd6196 (2022).
  - [17] H. Yoest, J. Buggeln, M. Doan, P. Johnson, S. A. Berman, K. A. Mitchell, and T. H. Solomon, Barriers impeding active mixing of swimming microbes in a hyperbolic flow, *Front. Phys.* **10**, 861616 (2022).
  - [18] K. C. Leptos, J. S. Guasto, J. P. Gollub, A. I. Pesci, and R. E. Goldstein, Dynamics of enhanced tracer diffusion in suspensions of swimming eukaryotic microorganisms, *Phys. Rev. Lett.* **103**, 198103 (2009).

- [19] A. Sokolov, I. S. Aranson, J. O. Kessler, and R. E. Goldstein, Concentration dependence of the collective dynamics of swimming bacteria, *Phys. Rev. Lett.* **98**, 158102 (2007).
- [20] R. Alert, J. Casademunt, and J.-F. Joanny, Active turbulence, *Annu. Rev. Condens. Matter Phys.* **13**, 143 (2022).
- [21] X.-L. Wu and A. Libchaber, Particle diffusion in a quasi-two-dimensional bacterial bath, *Phys. Rev. Lett.* **84**, 3017 (2000).
- [22] Y. Peng, Z. Liu, and X. Cheng, Imaging the emergence of bacterial turbulence: Phase diagram and transition kinetics, *Sci. Adv.* **7**, eabd1240 (2021).
- [23] C. Dombrowski, L. Cisneros, S. Chatkaew, R. E. Goldstein, and J. O. Kessler, Self-concentration and large-scale coherence in bacterial dynamics, *Phys. Rev. Lett.* **93**, 098103 (2004).
- [24] S.-Z. Lin, W.-Y. Zhang, D. Bi, B. Li, and X.-Q. Feng, Energetics of mesoscale cell turbulence in two-dimensional monolayers, *Commun. Phys.* **4**, 21 (2021).
- [25] W. K. Dewar, R. J. Bingham, R. Iverson, D. P. Nowacek, L. C. St Laurent, and P. H. Wiebe, Does the marine biosphere mix the ocean?, *J. Mar. Res.* **64**, 541 (2006).
- [26] E. Kunze, J. F. Dower, I. Beveridge, R. Dewey, and K. P. Bartlett, Observations of biologically generated turbulence in a coastal inlet, *Science* **313**, 1768 (2006).
- [27] A. W. Visser, Biomixing of the oceans? *Science* **316**, 838 (2007).
- [28] E. Kunze, Biologically generated mixing in the ocean, *Annu. Rev. Mar. Sci.* **11**, 215 (2019).
- [29] K. Katija, Biogenic inputs to ocean mixing, *J. Exp. Biol.* **215**, 1040 (2012).
- [30] I. A. Houghton, J. R. Koseff, S. G. Monismith, and J. O. Dabiri, Vertically migrating swimmers generate aggregation-scale eddies in a stratified column, *Nature (London)* **556**, 497 (2018).
- [31] R. Ouillon, I. Houghton, J. Dabiri, and E. Meiburg, Active swimmers interacting with stratified fluids during collective vertical migration, *J. Fluid Mech.* **902**, A23 (2020).
- [32] X. Si and L. Fang, Biologically generated turbulent energy flux in shear flow depends on tensor geometry, *PNAS Nexus* **3**, pgae056 (2024).
- [33] A. Attanasi, A. Cavagna, L. Del Castello, I. Giardina, T. S. Grigera, A. Jelić, S. Melillo, L. Parisi, O. Pohl, E. Shen, *et al.*, Information transfer and behavioural inertia in starling flocks, *Nat. Phys.* **10**, 691 (2014).
- [34] H. Ling, G. E. McIvor, J. Westley, K. Van der Vaart, J. Yin, R. T. Vaughan, A. Thornton, and N. T. Ouellette, Collective turns in jackdaw flocks: kinematics and information transfer, *J. R. Soc. Interface* **16**, 20190450 (2019).
- [35] N. T. Ouellette, H. Xu, and E. Bodenschatz, A quantitative study of three-dimensional lagrangian particle tracking algorithms, *Exp. Fluids* **40**, 301 (2006).
- [36] D. H. Kelley and N. T. Ouellette, Onset of three-dimensionality in electromagnetically driven thin-layer flows, *Phys. Fluids* **23**, 045103 (2011).
- [37] L. Fang and N. T. Ouellette, Influence of lateral boundaries on transport in quasi-two-dimensional flow, *Chaos* **28**, 023113 (2018).
- [38] N. T. Ouellette, P. J. J. O'Malley, and J. P. Gollub, Transport of finite-sized particles in chaotic flow, *Phys. Rev. Lett.* **101**, 174504 (2008).
- [39] D. Vella and L. Mahadevan, The “cheerios effect”, *Am. J. Phys.* **73**, 817 (2005).
- [40] L. Fang and N. T. Ouellette, Multiple stages of decay in two-dimensional turbulence, *Phys. Fluids* **29**, 111105 (2017).
- [41] G. Boffetta and R. E. Ecke, Two-dimensional turbulence, *Annu. Rev. Fluid Mech.* **44**, 427 (2012).
- [42] R. H. Kraichnan, Inertial ranges in two-dimensional turbulence, *Phys. Fluids* **10**, 1417 (1967).
- [43] G. Haller, Lagrangian coherent structures, *Annu. Rev. Fluid Mech.* **47**, 137 (2015).
- [44] G. Haller, A. Hadjighasem, M. Farazmand, and F. Huhn, Defining coherent vortices objectively from the vorticity, *J. Fluid Mech.* **795**, 136 (2016).
- [45] S. B. Pope and S. B. Pope, *Turbulent Flows* (Cambridge University Press, Cambridge, UK, 2000).
- [46] S. Balasuriya, R. Kalampattel, and N. T. Ouellette, Hyperbolic neighbourhoods as organizers of finite-time exponential stretching, *J. Fluid Mech.* **807**, 509 (2016).
- [47] M. Olascoaga, I. Rypina, M. Brown, F. Beron-Vera, H. Kocak, L. Brand, G. Halliwell, and L. Shay, Persistent transport barrier on the west florida shelf, *Geophys. Res. Lett.* **33**, 2006GL027800 (2006).